Electronic Supplementary Material (ESI) for Journal of Materials Chemistry A.

Mitigating Oxygen Release in Anionic-Redox-Active Cathode Materials by Cationic Substitution through Rational Design

Thomas A. Wynn[a], Chengcheng Fang[a], Minghao Zhang[b], Haodong Liu[b], Daniel M. Davies[b], Xuefeng Wang[b], Derek Lau[b], Jungwoo Z. Lee[b], Bo-Yuan Huang[c], Kuan-Zong Fung[c], Chung-Ta Ni[c], Ying Shirley Meng[a,b,d]*

a. Materials Science and Engineering Program, University of California San Diego, La Jolla, CA 92093, USA

b. Department of Nanoengineering, University of California San Diego, La Jolla, CA 92093, USA

c. Department of Materials Science and Engineering, National Cheng Kung University, Tainan 70101, Taiwan, ROC

d. Sustainable Power and Energy Center, University of California San Diego, La Jolla, CA 92093, USA

*e-mail: shirleymeng@ucsd.edu

Full structural model description

For brevity, a complete description of the model was omitted from the full text. A number of considerations were put into the development of a model for the incorporation of a dopant into the $Li_{12}[Li_2Ni_3Mn_7]O_{24}$ supercell. First, the location of the dopant may vary between doping cases. As a rule of thumb, delithiation and E^F_{Ov} calculations were performed on the lowest energy configuration for each dopant scenario. It should be noted that the local environment of a particular oxygen vacancy does not necessarily contain the same local environment across dopants. Similarly, the incorporation of a dopant is naturally accompanied by an increased variety of local environments (Figure S1c). However, the general trends to remain the same: in the relaxed structure, the oxygen vacancy near a combination of a nickel atom, a transition metal layer lithium vacancy, and a lithium-layer lithium that has migrated to a tetrahedral dumbbell site consistently produces the lowest E^F_{Ov} site. Delithiation to $Li_7[LiNi_3Mn_6M]O_2$ results in further increase in types of local bonding environments. Figure S1a,b serves to aid in visualization of some representative oxygen environments as described in the Figure 2 of the manuscript.

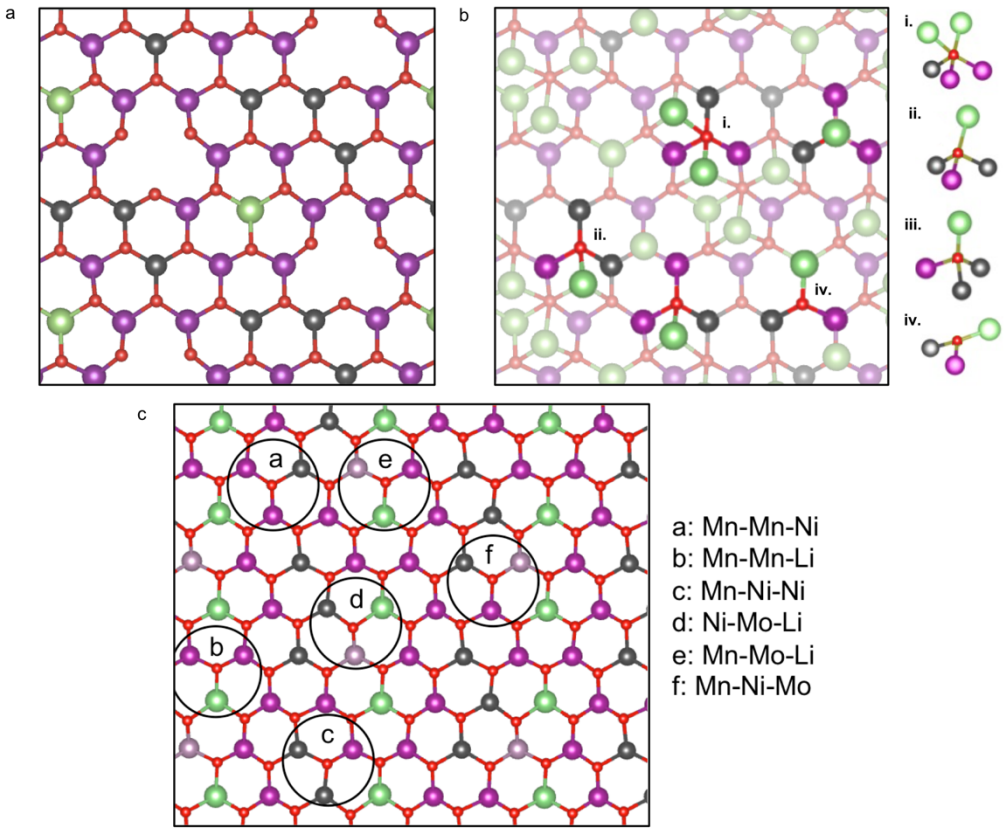

Figure S1: In isolated view of the transition metal layer in the lithiation state 8/14; (b) the same layer with lithium-layer lithium ions forming local coordinations around oxygen ions. Incorporation of dopants introduces a wider range local bonding environments. The Mo-doped structure is shown as an example (Li: green, Mn: purple, Ni: black, Mo: grey).

Mott-Hubbard values used in the GGA+*U* calculations in this work are provided in Table S1 below. It is apparent that the *+U* parameter may have a drastic impact on the results of density functional theory calculations. Care was taken to use well-established values these cases, and where not established for energy storage materials, follow literature values with experimentally confirmed values.

Table S1: Mott-Hubbard values and references used in the *+U* calculations in this work.[1–10]

	$+U_{eff}$	Ref.		$+U_{eff}$	Ref.
Sc	7	1	Ni	6	4
Ti	5.2	2	Y	5.08	6
V	5	3	Zr	3	7
Mn	6.96	4	Nb	3.07	8
Fe	5.3	5	Mo	3.5	9
Co	5.91	5	Ru	4	10

Calculation results in the context of oxygen redox

As shown in previous work, the notion of labile oxygen is observed computationally through he increased density of states below the Fermi level of oxygen atoms coordinated with TM layer lithium. This work, having used GGA+*U* similarly shows an increased oxygen density of states below the Fermi level for oxygen with a linear Li-O-Li bond (Figure S2b), suggesting that electronic structure for oxygen redox is still observable using the GGA+*U* functional. Conversely, oxygen sites lacking the Li-O-Li bond lack this delocalized density (Figure S2a).

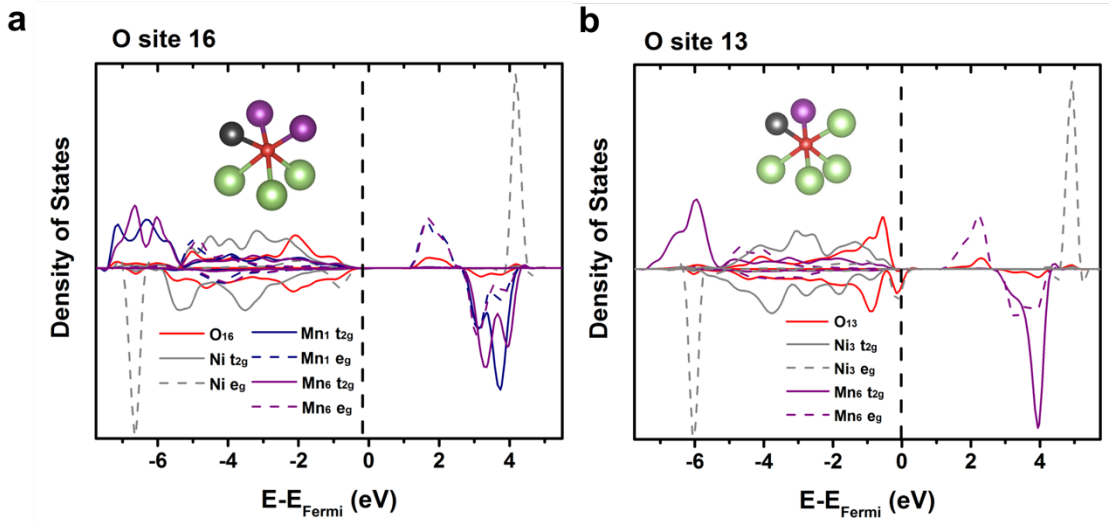

Figure S2: An example of an oxygen site in the fully lithiated structure (a) without a Li-O-Li linear bond and (b) with a Li-O-Li linear bond, required for labile oxygen states. The presence of the Li-O-Li linear configuration shows a greatly increased 2p density of states within 1.5 eV of the Fermi energy.

Bader charge analysis

Although unable to quantitatively determine oxidation states, Bader charge analysis is useful for examining trends in charge density behavior. Table S2 displays the Bader charge for the delithiated state and the change in Bader charge after delithiation. Previous *ab initio* work operated under the assumption that oxygen sites with the lowest Bader charge is the most likely to evolve, though under Mo-doping there exists a discrepancy between the lowest E_{Ov}^{F} site (oxygen site 13) and the site with the lowest charge and largest change (oxygen site 5). Analysis was performed using a grid-based method as described in reference.[11]

Table S2: Bader charge difference between lithiated and delithiated states for undoped and doped materials. Items in bold are sites exhibiting the lowest Bader charge and the largest change in Bader charge.

O Site	Bader Charge (Delithiated)					Δ Bader Charge (Pristine – Delithiated)				
	NM	Al	Ti	Co	Mo	NM	Al	Ti	Co	Mo
1	6.87	6.86	6.86	6.78	7.04	0.29	0.30	0.31	0.33	0.13
2	6.98	6.96	7.09	6.98	6.92	0.19	0.21	0.17	0.19	0.29
3	6.92	6.92	6.94	6.92	7.01	0.27	0.19	0.26	0.27	0.19
4	6.97	7.11	6.97	6.97	6.97	0.17	0.22	0.17	0.17	0.25
5	6.88	6.87	6.88	6.83	**6.84**	0.32	0.32	0.32	0.31	**0.36**
6	6.99	7.14	7.02	7.00	7.03	0.17	0.21	0.14	0.16	0.13
7	7.00	6.97	6.99	7.00	7.02	0.16	0.20	0.17	0.16	0.15
8	7.09	7.09	7.10	7.04	7.11	0.10	0.10	0.09	0.10	0.13
9	6.99	6.98	6.99	6.99	6.98	0.18	0.19	0.18	0.18	0.17
10	6.98	6.99	7.00	6.97	7.02	0.17	0.15	0.23	0.18	0.23
11	7.04	7.20	7.04	7.04	7.06	0.10	0.16	0.11	0.10	0.09
12	**6.92**	**6.91**	**7.04**	**6.94**	6.98	**0.32**	**0.24**	**0.29**	**0.30**	0.23
13*	6.76	6.74	6.75	6.71	6.97	0.47	0.40	0.49	0.46	0.29
14	7.02	7.01	7.09	7.02	7.04	0.16	0.17	0.17	0.16	0.20
15	7.04	7.04	7.00	7.04	7.06	0.11	0.10	0.15	0.11	0.08
16	6.93	7.07	6.93	6.93	6.91	0.21	0.26	0.21	0.21	0.22
17	6.84	6.83	6.83	6.84	6.87	0.36	0.26	0.36	0.36	0.33
18	7.03	7.15	7.03	7.03	7.06	0.14	0.23	0.15	0.15	0.13
19	7.02	7.00	7.03	6.95	7.04	0.13	0.17	0.13	0.16	0.13
20	6.95	6.95	6.95	6.90	6.88	0.22	0.22	0.22	0.23	0.33
21	7.15	7.15	7.16	7.16	7.15	0.04	0.04	0.03	0.03	0.03
22	6.92	7.10	6.95	6.92	7.03	0.21	0.22	0.19	0.22	0.15
23	7.03	7.01	7.13	7.02	7.05	0.13	0.15	0.12	0.14	0.12
24	6.90	6.89	7.00	6.91	6.99	0.31	0.32	0.31	0.31	0.29

Oxidation State Calculations

Oxidation states of the transition metals before and after delithiation were determined from the magnetization output of the DFT simulations (Table S3). Undoped simulations show fully oxidized Mn^{4+}, with $Ni^{2+/3+}$ available for redox. Incorporation of typical dopants Al, Co, and Ti show no impact on this redox behavior. Though incorporation of Mo predicts that Mo will be incorporated as Mo^{5+}, with some Mn in the Mn^{3+} state.

Table S3: Impact of dopant on oxidation state change on delithiation and oxygen removal of redox-active ions, as measured by simulated magnetizations. The multiplier refers to instances of the redox change within a single supercell.

Dopant	Theoretical Redox Change	
No dopant	$Ni^{2+} \rightarrow Ni^{3+}$	x 2
	$Ni^{2+} \rightarrow Ni^{4+}$	x 1
Al	$Ni^{2+} \rightarrow Ni^{3+}$	x 2
	$Ni^{2+} \rightarrow Ni^{4+}$	x 1
Co	$Ni^{2+} \rightarrow Ni^{3+}$	x 2
	$Ni^{2+} \rightarrow Ni^{4+}$	x 1
Mo	$Ni^{2+} \rightarrow Ni^{3+}$	x 2
	$Mn^{3+} \rightarrow Mn^{4+}$	x 1
	$Mo^{5+} \rightarrow Mo^{6+}$	x 1

Electrochemical Impedance Spectroscopy

Electrochemical impedance spectroscopy (EIS) measurements are conducted to investigate the influence of Mo doping on electrochemical behavior, including electronic conductivity and bulk ion diffusion. Before cycling, both LNMLO-Co and LNMLO-CoMo cells show relatively larger charge transfer impedance than that of after cycling, as a formation cycle is needed to reduce the overall resistance. At OCV state, both cells only show one semicircle, which represents charge transfer resistance (R_{CT}). After 30 cycles, an SEI is formed on the surface of cathode materials, and an additional semicircle can be measured at high frequency region, representing resistance of SEI film (R_{SEI}). W is the Warburg impedance related to bulk lithium ion diffusion. The fitting values are listed in Table S4. Mo-doped sample shows reduced R_{CT} before and after cycling, and much smaller R_{SEI} after 30 cycles. It is clearly shows in Figure S3 that after Mo doping, the material exhibits much reduced impedance and improved ionic diffusion. Table S4 lists the quantitatively fitting results of both materials before and after cycling.

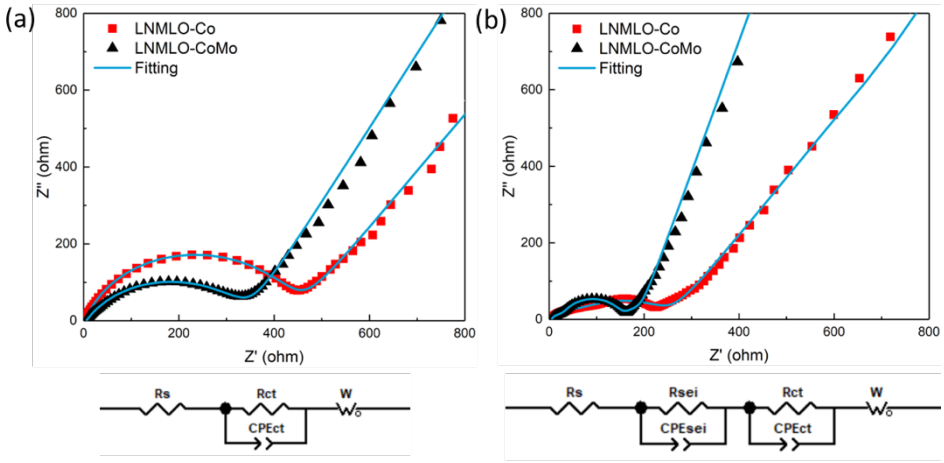

Figure S3: Nyquist plots of LNMLO-Co and LNMLO-CoMo (a) at OCV and (b) after 30 cycle, with corresponding fitting circuits (below).

Table S4: EIS fitting results of LNMLO-Co and LNMLO-CoMo at OCV and after 30 cycle

	LNMLO-Co 0 Cycles	LNMLO-CoMo 0 Cycles	LNMLO-Co 30th Cycle	LNMLO-CoMo 30th Cycle
R_S (Ω)	3.662	5.787	4.584	4.965
R_{SEI} (Ω)	–	–	44.52	24.72
R_{CT}(Ω)	436.4	339.5	210.3	111

Doping and electrochemistry of Al- and Ti-doped LRLO

Al and Ti were chosen to verify the negligible impact on oxygen evolution as observed by the electrochemical performance of LNMLO, according to calculation prediction. Numerous studies have doped Al and Ti in a range of concentrations, each with varying results.[12–14] In spite of discrepancies in optimal doping concentrations, a small amount of substitution (1%, 2%) consistently shows notable deviations from the undoped cases. With the intent to prevent possible surface coating effects from excess dopant content, 2% Al (LNMLO-Al) and 1% Ti (LNMLO-Ti) doping into LNMLO is performed to re-evaluate the impact of doping in terms of oxygen behavior. Al-doped $Li[Li_{0.2}Ni_{0.19}Mn_{0.59}Al_{0.02}]O_2$ (LNMLO-Al) and Ti-doped $Li[Li_{0.2}Ni_{0.2}Mn_{0.59}Ti_{0.01}]O_2$ (LNMLO-Ti) lithium rich layered oxide cathode materials were prepared through hydroxide co-precipitation method (OHCP). Synthesis of TM (Ni, Mn) hydroxide precursors was detailed in our previous work.[15–17] Then the as-prepared TM precursors were mixed with a stoichiometric amount of $LiOH{\cdot}H_2O$ and Al_2O_3 (for Al-doped sample). Ti was incorporated during co-precipitation process by using $Ti(OC_4H_9)_4$. After grinding for 30 minutes, the mixture was then annealed by two steps, 480 ^oC for 12 hours and 900 ^oC for 12 hours in air, to get the final product. In Figure S4(a) and (b), first charging curves of LNMLO-Al and LNMLO-Ti materials both show an oxygen plateau of a similar width to that of the undoped LNMLO. Specifically, the plateau length of LNMLO-Al and LNMLO-Ti are 212 and 206 mAh/g, respectively, near that of pristine LNMLO is 204 mAh/g, indicating Al and Ti doping have a weak influence on oxygen activities; this is in line with calculations, having shown little change in the lowest E_{Ov}^F site. Figure S4(c) and (d) show further evidence for the relatively small impact of Al and Ti doping, exhibiting similar voltage decay to the undoped material after 100 cycles. The average voltage retention of LNMLO-Al, LNMLO-Ti and LNMLO are 96.7%, 96.2% and 96.4%, respectively, indicating little change after Al and Ti doping. However, it is worth mentioning that our conclusions on Al and Ti doping into lithium rich layered oxides are not in agreement with most previous studies, as variations of electrochemical performances were observed after doping in these other works. For instance, Nayak *et al.* reported that doping $Li_{1.2}Ni_{0.16}Mn_{0.56}Co_{0.08}O_2$ by Al results in a decreased capacity but improved cycling stability, as well as reduced average discharge voltage decay.[14] As mentioned before, Wang *et al.*'s and Deng *et al.*'s experimental work also shows that higher substitution amounts (6-20%) of Al and Ti doping lead to a suppression of oxidation of O^{2-} ions to oxygen.[12] Though based on both of our computational and experimental results, we speculate the more drastic changes in electrochemical behaviors in these previous works may to some extent be attributed to incomplete dopant incorporation and subsequent surface effects.

To verify the phase purity and observe structure changes of as-synthesized materials, X-ray diffraction and subsequent Rietveld refinement were performed (Figure S5). For LNMLO-Al, two dopant ions per formula unit substitutes one Ni^{2+} (0.69 Å) and one Mn^{4+} (0.53 Å) to maintain charge balance during synthesis. The decreased lattice parameters of LNMLO-Al can be ascribed to the smaller ionic radius of Al^{3+} (0.535 Å). Accordingly, the refined experimental a-lattice parameter of LNMLO-Ti does not show obvious change compared with that of undoped LNMLO. Variation in structural parameters with cation substitution was also calculated by DFT (Table S5). It was predicted that Al-doping results in a slight contraction lattice

parameters, showing reduced bond lengths in the MO_6 octahedron. Further consistent with experiment, Ti is predicted to expand the *c* lattice parameter, due to the increased Ti-O bond lengths relative to the replaced Mn-O bond lengths. As shown in Figure S5 and Table S5, experimental fittings show these values to generally follow the predicted trends. The XRD results suggest Al and Ti have been successfully doped into the structure.

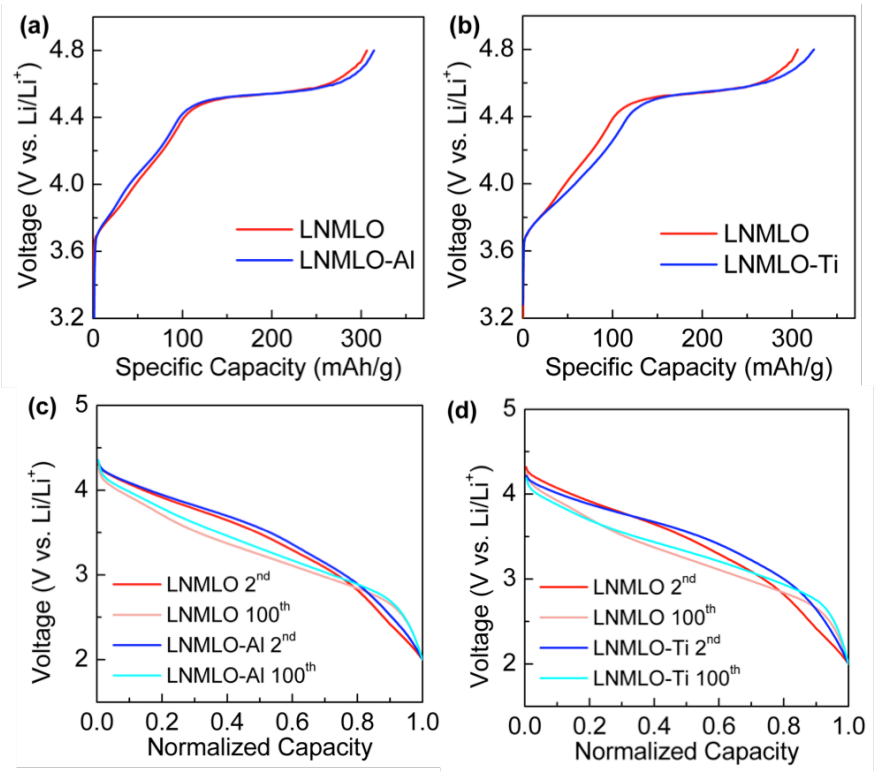

Figure S4: (a) First charging profiles of LNMLO-Al and LNMLO-Ti materials, compared with pristine LNMLO. Oxygen plateau length of doped materials is similar to that of pristine material, commensurate with DFT calculations. (b) LNMLO-Al, LNMLO-Ti and LNMLO show similar voltage decay after 100 cycles, indicating Al- and Ti- doping does not have influence on electrochemical performance.

Table S5: Lattice parameters from DFT calculation (Theoretical) and from Rietveld refinement (Experimental) for Al and Ti doping.

	Theoretical		Experimental	
	a = b (Å)	c (Å)	a = b (Å)	c (Å)
Undoped	2.908	14.435	2.8600(7)	14.241(3)
Al	2.897	14.421	2.8548(8)	14.235(4)
Ti	2.907	14.482	2.8599(1)	14.253(2)

X-ray diffraction

To observe structural change and verify phase purity, X-ray diffraction and subsequent Rietveld refinement were performed on all samples studied in this paper. The experimental observations of lattice parameters variation for LNMLO-Co, LNMLO-CoMo, LNMLO-Al, and LNMLO-Ti, match well with DFT calculation prediction, indicating all dopants have been successfully incorporated into the pristine NM structure. For Mo, 1% is the saturate point of doping according to previous study.[18] Consistently in the present work, 3% of doping shows impurity peaks.

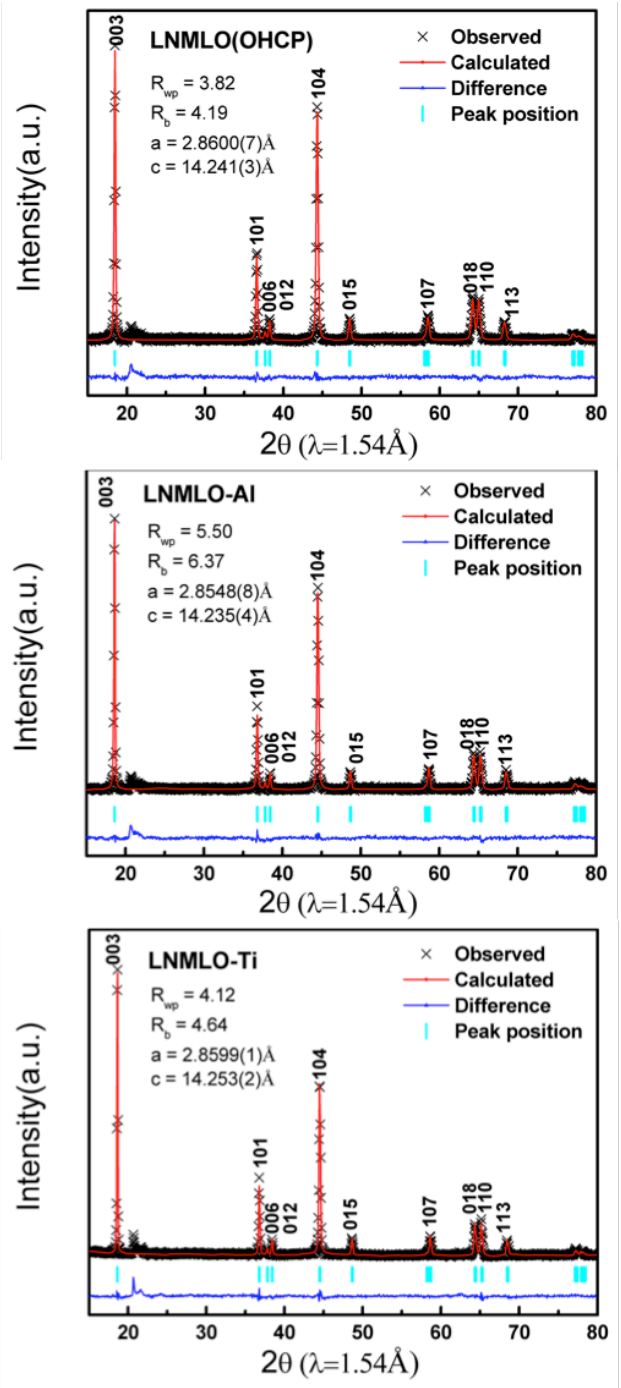

Figure S5: X-ray diffraction and Rietveld refinement of LNMLO, LNMLO-Al, and LNMLO-Ti. LNMLO-Al shows decreased a- and c- lattice parameters due to the smaller ionic radius of Al^{3+}; LNMLO-Ti exhibits similar a-, but much higher c-, comparing with LNMLO.

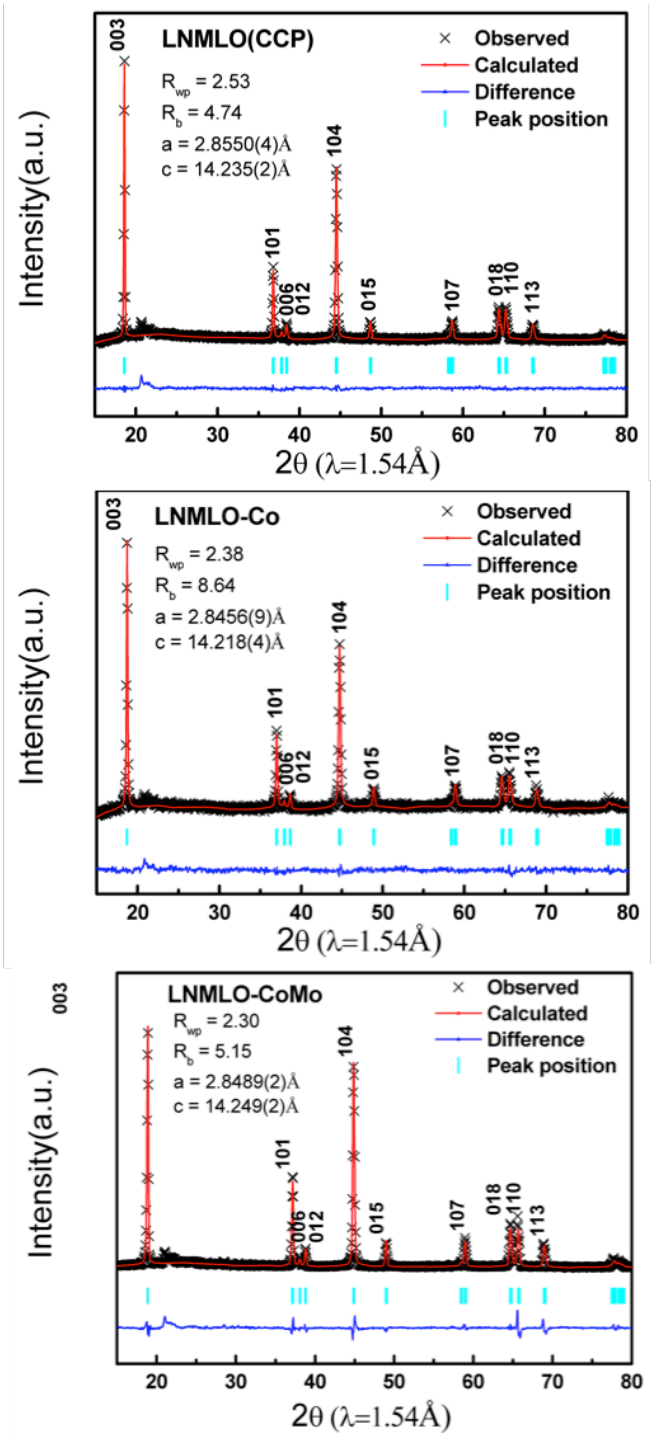

Figure S6: X-ray diffraction and Rietveld refinement of LNMLO, LNMLO-Co, LNMLO-CoMo. As the ionic radius of Co^{3+} is smaller than Ni^{2+} and close to Mn^{4+}, NMC shows shrink lattice parameters. After 1% of Mo doping, both *a*- and *c*- of LNMLO-CoMo increase compared with LNMLO-Co, indicating Mo has been successfully doped into LNMLO-Co structure.

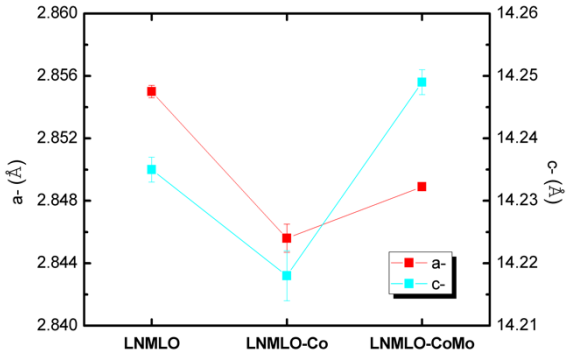

Figure S7: Lattice parameters of LNMLO, LNMLO-Co and LNMLO-CoMo as determined by Rietveld refinement of XRD spectra (Figure S6).

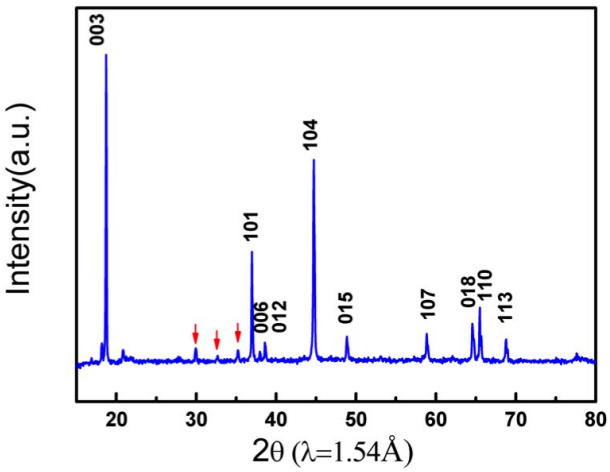

Figure S8: 3% Mo-doping shows the presence of impurity peaks in XRD.

Evidence of uniform doping distribution

To confirm the uniformity of Mo distribution, focused ion beam cross-sections of secondary particles was performed, allowing a clear view of the distribution of transition metal ions through profiles of the primary particles. Using energy dispersive x-ray spectroscopy, a uniform distribution of all TMs is observed, suggesting that the Mo dopant is uniformly distributed throughout the bulk of the material.

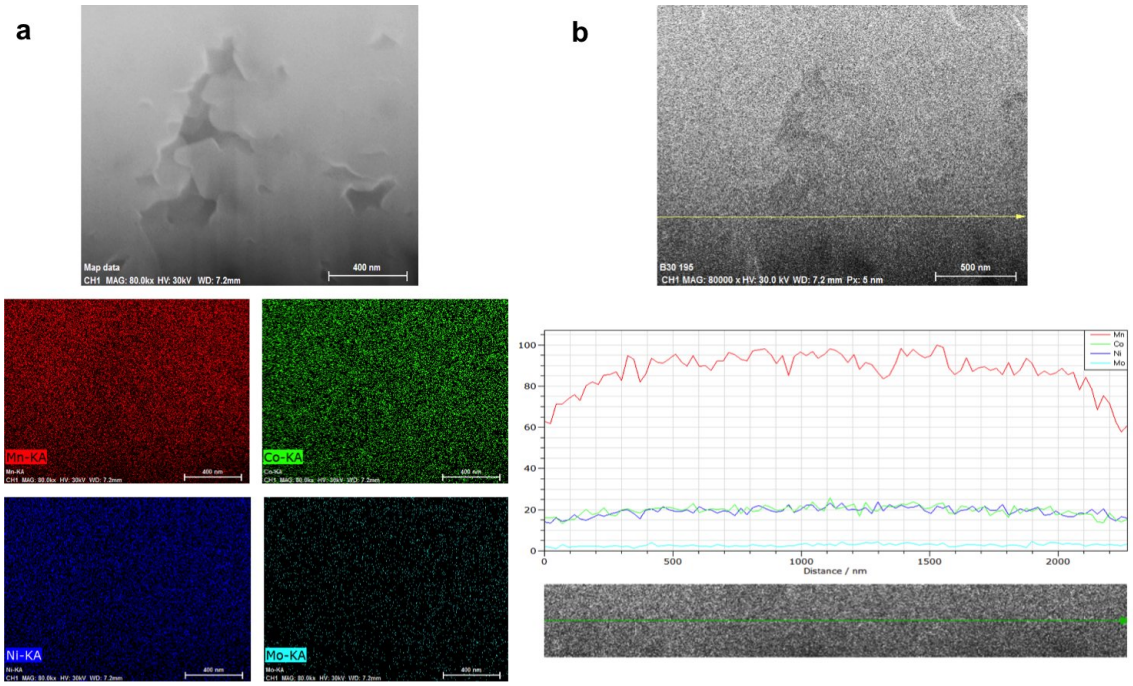

Figure S9: Energy dispersive x-ray spectroscopy was performed on a focused ion beam cross-section of a secondary particle of the Mo-doped material. (a) The Mo map suggests that the Mo is evenly disbursed, further evidence of incorporation into the structure. (b) Similarly, a higher resolution line-scan shows no accumulation at primary particle boundaries and surfaces.

Mo-doping of Li_2MnO_3 similarly shows improved capacity retention

Mo-doped material $Li_2Mn_{1-x}Mo_xO_3$ was prepared by a typical sol-gel method. Lithium acetate, manganese acetate and ammonium heptamolybdate precursors were mixed and heated up to 100 °C until a gel-like solution formed. The gel precursor was calcined at 600 °C for 6 hr to obtain the $Li_2Mn_{1-x}Mo_xO_3$ cathode powder. Mo doping of x=0, 2.5, and 5.0 were synthesized, characterized by XRD (Figure S10), and cycled (Figure S11). Cycling data shows notably improved capacity retention with increased amount of Mo dopant, further supporting the ability of Mo to prevent oxygen vacancy formation.

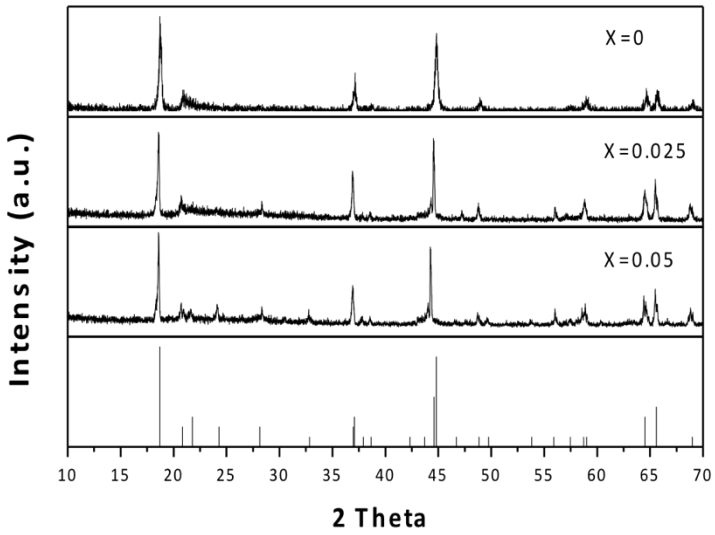

Figure S10: X-ray diffraction of $Li_2Mn_{1-x}Mo_xO_3$ at dopant concentrations of x=0, 0.025, and 0.05 show incorporation of the dopant without the formation of impurities.

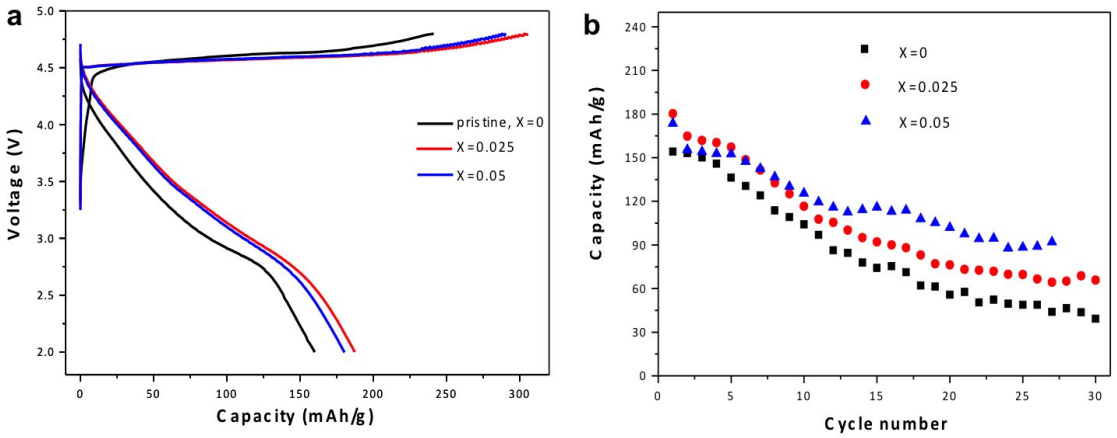

Figure S11: (a) First cycling data of $Li_2Mn_{1-x}Mo_xO_3$ at dopant concentrations of x=0, 0.025, and 0.05; (b) incorporation of Mo shows an improvement in capacity retention with increased Mo concentration.

References

1 M. B. Kanoun, S. Goumri-Said, U. Schwingenschlogl and A. Manchon, *Chem. Phys. Lett.*, 2012, **532**, 96–99.

2 B. J. Morgan and G. W. Watson, *Surf. Sci.*, 2007, **601**, 5034–5041.

3 D. O. Scanlon, A. Walsh, B. J. Morgan and G. W. Watson, *J. Phys. Chem. C*, 2008, **112**, 9903–9911.

4 Y. Hinuma, Y. S. Meng, K. Kang and G. Ceder, *Chem. Mater.*, 2007, **19**, 1790–1800.

5 V. L. Chevrier, S. P. Ong, R. Armiento, M. K. Y. Chan and G. Ceder, *Phys. Rev. B*, 2010, **82**, 075122.

6 J. Feng, S. Shian, B. Xiao and D. R. Clarke, *Phys. Rev. B*, 2014, **90**, 1–13.

7 G. Y. Huang, C. Y. Wang and J. T. Wang, *Comput. Phys. Commun.*, 2012, **183**, 1749–1752.

8 H. Kamisaka, T. Hitosugi and K. Yamashita, *Hyomen Kagaku*, 2010, **31**, 343–351.

9 M. Khan, J. N. Xu, N. Chen and W. B. Cao, *Phys. B-Condensed Matter*, 2012, **407**, 3610–3616.

10 P.-A. Lin, H.-T. Jeng and C.-S. Hsue, *Phys. Rev. B*, 2008, **77**, 085118.

11 W. Tang, E. Sanville and G. Henkelman, *J. Phys. Condens. Matter*, 2009, **21**, 084204.

12 C.-C. Wang and A. Manthiram, *J. Mater. Chem. A*, 2013, **1**, 10209–10217.

13 M. Iftekhar, N. E. Drewett, A. R. Armstrong, D. Hesp, F. Braga, S. Ahmed and L. J. Hardwick, *J. Electrochem. Soc.*, 2014, **161**, A2109–A2116.

14 P. K. Nayak, J. Grinblat, M. Levi, E. Levi, S. Kim, J. W. Choi and D. Aurbach, *Adv. Energy Mater.*, 2016, **6**, 1502398.

15 H. Liu, D. Qian, M. G. Verde, M. Zhang, L. Baggetto, K. An, Y. Chen, K. J. Carroll, D. Lau, M. Chi, G. M. Veith and Y. S. Meng, *ACS Appl. Mater. Interfaces*, 2015, **7**, 19189–19200.

16 H. Liu, C. R. Fell, K. An, L. Cai and Y. S. Meng, *J. Power Sources*, 2013, **240**, 772–778.

17 M. G. Verde, H. Liu, K. J. Carroll, L. Baggetto, G. M. Veith and Y. S. Meng, *ACS Appl. Mater. Interfaces*, 2014, **6**, 18868–18877.

18 Y. Zang, C.-X. Ding, X.-C. Wang, Z.-Y. Wen and C.-H. Chen, *Electrochim. Acta*, 2015, **168**, 234–239.